ACS APPLIED MATERIALS & INTERFACES

ACS EDITORS' CHOICE

www.acsami.org

Research Article

Atomic-Scale Imprinting by Sputter Deposition of Amorphous Metallic Films

Zheng Chen, Amit Datye, Georg H. Simon, Chao Zhou, Sebastian A. Kube, Naijia Liu, Jingbei Liu, Jan Schroers, and Udo D. Schwarz*

Cite This: *ACS Appl. Mater. Interfaces* 2020, 12, 52908−52914

Read Online

ACCESS | Metrics & More | Article Recommendations

ABSTRACT: With its ease of implementation, low cost, high throughput, and excellent feature replication accuracy, nanoimprinting is used to fabricate structures for electrical, optical, and biological applications or to modify surface properties. If ultraprecise and/or subnanometer-sized patterns are desired, nanoimprinting has shown only limited success with polymers, silica glasses, or crystalline materials. In contrast, the absence of an intrinsic length scale that would interfere with imprinting resolution enables bulk metallic glasses (BMGs) to replicate structures down to the atomic scale through thermoplastic forming (TPF). However, only a small number of BMG-forming alloys can be used for TPF-based atomic-scale imprinting. Here, we demonstrate an alternative sputter deposition-based approach for the replication of atomic-scale features that is suited for a very broad range of amorphous alloys, thereby dramatically extending the available chemistries. Additional advantages are the method's scalability, its ability to replicate a wide range of molds, its low material consumption, and the fact that the films can readily be applied onto almost any workpiece, which together open up new avenues to atomically defined surface structuring and functionalization. Our method constitutes the advancement from proof of concept to a practical and highly versatile toolbox of atomic-scale imprinting to be explored for the science and technology of atomic-scale imprinting.

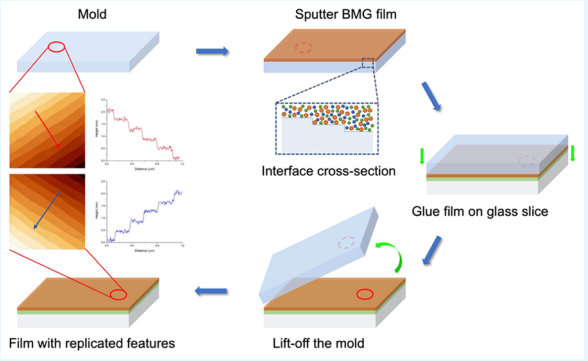

KEYWORDS: *atomic-scale replication, nanoimprinting, metallic glasses, physical vapor deposition, surface functionalization*

INTRODUCTION

Nanoimprinting has gathered attention in recent decades as a way to achieve nanostructured surfaces relevant for a wide range of applications,[1,2] including high-density data storage,[3] photonic devices,[4−6] holograms,[7] bionanofluidic chips,[8] sensing,[9,10] manipulation of cellular response,[11,12] water filtration,[13] and electrodes in fuel cells.[14] Key parameters in nanoimprinting are the size of the smallest reproducible structural features and the smoothness of the exposed surfaces. Even though a broader range of techniques and materials exist that allow embossing patterns with dimensions of the order of 100 nm,[13,15,16] producing single-digit nanoscale features or even structures with subnanometer dimensions has remained challenging.[2,17−20] For polymers and oxide glasses, this has in principle been demonstrated even though intricacies were often lacking: the replicated structures were typically simple features showing considerable roughness.[21−26] In the case of polymers, the chain size was concluded to introduce a natural lower limit for quality replication around 1−5 nm.[13,19] Nevertheless, metals and metallic alloys are often more desired for nanopatterned surfaces because of their functional properties such as catalytic activity, plasma frequency, reflexivity, and mechanical strength.

More recently, the molding of subnanometer size features into bulk metallic glasses (BMGs) using thermoplastic forming (TPF) was demonstrated.[7,27−30] For example, when using single-crystalline strontium titanate (STO) as a mold, the imprinted BMG sample exhibits an exact mirror image of the terraced surface structure of the STO (step heights between terraces ≈0.39 nm) with identical subangstrom on-terrace roughness, suggesting atom sizes, interatomic distances, and packing polyhedra as the only factors limiting the imprint feature size.[29]

Because of the specific requirements of atomic-scale imprinting by TPF such as stability at processing temperatures and pressures, favorable time- and temperature-dependent

Received: August 20, 2020
Accepted: October 16, 2020
Published: November 16, 2020

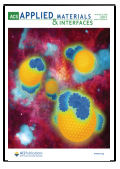

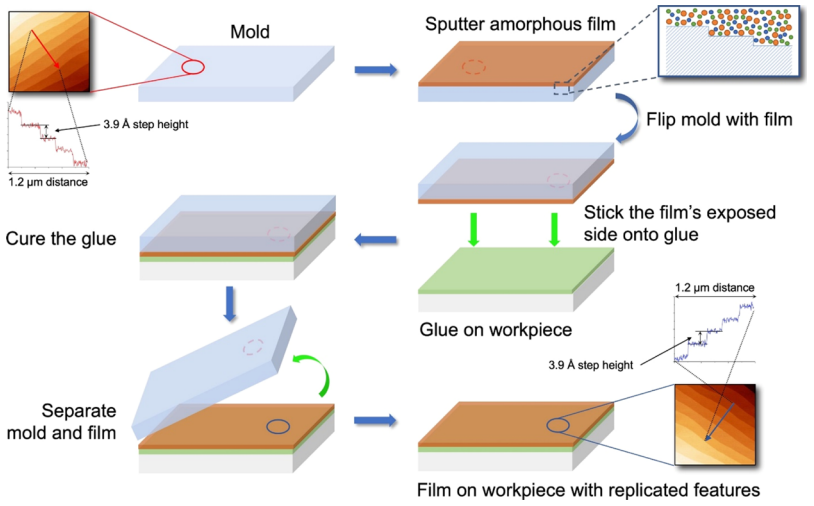

Figure 1. Schematic step-by-step illustration of the replication and film transfer process. First, a mold with angstrom-size features is introduced into a sputtering system. An atomic force microscopy (AFM) image of a (001)-oriented $SrTiO_3$ single crystal that exhibits atomically flat terraces separated by unit cell high steps of 3.9 Å and a related line section are displayed as an example. A desired glass-forming alloy film is then sputter deposited that grows to conform with the mold's atomic-scale features at the mold-film interface (cf. the schematic cross section in the upper-right featuring a three-component film with orange, green, and blue atoms). Once deposition is complete, the mold/film stack is flipped over and attached with epoxy glue to a workpiece of choice. Separation from the mold can then easily be achieved mechanically, with the then-exposed surface showing an inverted mirror image of the original mold pattern.

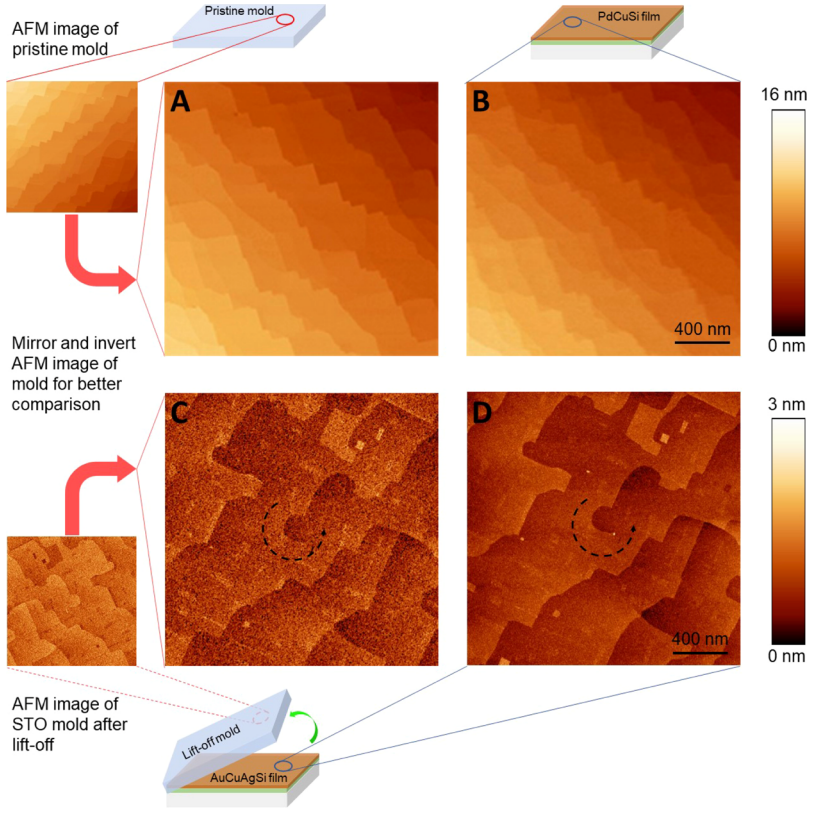

Figure 2. Results from two case studies that exemplify the replication fidelity of the method. To characterize the mold used in case study 1, an STO crystal prepared as described in the Materials and Methods section, we imaged it by AFM before its introduction into the sputtering system ("pristine mold"), with the related AFM image depicted in the upper-left inset. A mirrored and inverted version of this original AFM image is then displayed in (A) to ease comparison with the replica film, which was formed by sputter depositing $Pd_{75.5}Cu_6Si_{18.5}$. The AFM image in panel (B) reflects the location on this replica that is equivalent to the one shown in (A) for the mold, revealing subangstrom reproduction fidelity. (C,D) Case study 2 in a similar way, with panel (C) presenting a mirrored and inverted AFM image of the STO mold used to form the $Au_{50}Cu_{25.5}Ag_{7.5}Si_{17}$ film displayed in (D). This time, however, the mold was imaged after separation from the film. In addition, the location of a screw dislocation is highlighted in panels (C,D). All AFM images are 2 μm × 2 μm in size.

https://dx.doi.org/10.1021/acsami.0c14982
ACS Appl. Mater. Interfaces 2020, 12, 52908−52914

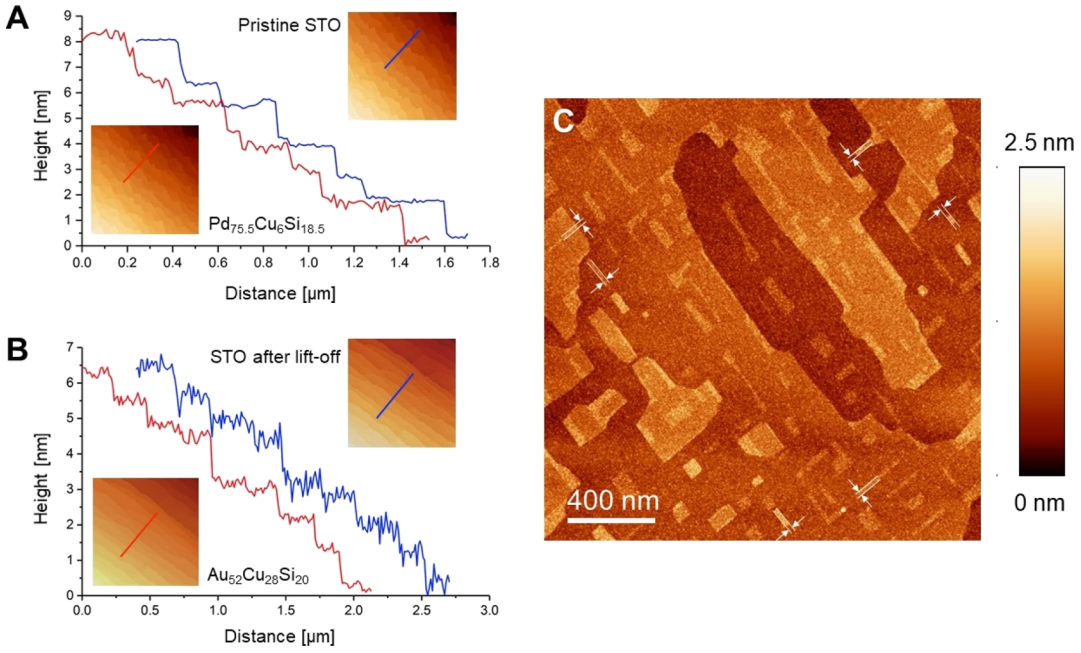

Figure 3. Analysis of vertical and lateral replication resolution. (A) Line profile curves of the STO mold (blue line) and a $Pd_{75.5}Cu_6Si_{18.5}$ film (red line) taken at the locations indicated in the AFM images shown as insets. Image sizes are 3 μm × 3 μm, with the image of the pristine STO again representing the mirrored and inverted version of the original data. When comparing the two curves, on-terrace height fluctuations are found to be only modestly higher on the replica than on the original mold. (B) Line profiles as in (A), but with the STO data (upper-right inset) recorded after separation from an $Au_{52}Cu_{28}Si_{20}$ film (lower-left inset), which results in the blue curve's enhanced on-terrace roughness. Inset images are each 5 μm × 5 μm in size. (C) AFM image of an $Au_{50}Cu_{25.5}Ag_{7.5}Si_{17}$ film. In this particular case, the STO crystal featured a number of elongated but narrow pits aligned with the [100] and [010] directions of the crystal's (001) surface which are appearing as rectangular protrusions on the replica. From measuring the width of a number of these, an upper limit for the smallest reproducible lateral feature of 20 nm can be established. To guide the eye, parallel lines 20 nm apart are highlighting dimensions of such stripes at different locations.

viscosity, inertness to oxidation during forming,[31] it is limited to a small subset of BMGs that currently includes only specific Pt-based BMGs.[29] To unleash the potential of atomic-scale imprinting from a proof of concept from a scientific curiosity to a widely used nanofabrication tool, we developed a novel process based on magnetron sputtering. This approach can be employed with a wide range of alloys,[32] which provides a large toolbox for selecting a desired surface chemistry while being extremely versatile in terms of size, shape, and nature of the surface pattern and of the molds that can be used.

RESULTS AND DISCUSSION

The protocol on how to achieve the atomic-scale imprinting presented here is illustrated in Figure 1. With details given in the caption, a mold with atomic-scale features (here: terraces on a $SrTiO_3$ single crystal separated by steps of unit cell height; upper-left) is covered by a sputter-deposited amorphous film (upper-right). This film can then be attached to a workpiece of choice; in our experiments, we glued it onto a glass slide (middle-right). Once the mold and the film are separated, the newly exposed surface of the film (lower-right) represents an exact mirror image of the original mold.

Figure 2 illustrates the subangstrom replication fidelity that can be achieved using this process when using STO single crystals as molds with two different cases. First, we compare AFM images recorded at equivalent positions on the pristine STO mold (i.e., before film growth was carried out) and on the resulting amorphous $Pd_{75.5}Cu_6Si_{18.5}$ film after it had been lifted off the mold. To facilitate the comparison, a mirrored and inverted version of the original AFM image is displayed in Figure 2A, with its step structures revealing an excellent match with its replica in Figure 2B.

To explore the method's versatility in the compositional space that is accessible, we used for the second case study a common glass former, $Au_{50}Cu_{25.5}Ag_{7.5}Si_{17}$, to produce a replica (Figure 2C,D). As before, Figure 2C represents a mirrored and inverted AFM image of an STO mold, but this time measured after the film has been lifted off, and Figure 2D depicts the $Au_{50}Cu_{25.5}Ag_{7.5}Si_{17}$ replica, recorded at the location that is equivalent to the one of Figure 2C. Despite a slightly higher apparent roughness on the surface of the STO mold than on the Au-based replica, which will be discussed further below in more detail, the step structures of Figure 2C,D reveal a high-fidelity match down to angstrom-height features on the terraces. For example, we find an impeccable replication of a screw dislocation terminating at the surface marked by circular arrows in the center of the images. Following these from the end to end, one can seamlessly move from a higher terrace to a lower one that is separated from the higher one by the step edge pointed out in (D) as the separating edge "disappears" where the dislocation line of the original mold has hit the surface.

For a quantitative analysis of the replication quality, we turn to Figure 3. First, replication with the $Pd_{75.5}Cu_6Si_{18.5}$ alloy is further examined in panel (A), which shows line profiles taken at equivalent locations on both the mirrored and inverted STO mold (blue line) and the $Pd_{75.5}Cu_6Si_{18.5}$ film (red line), demonstrating a near-perfect replication of both the step heights and the terrace widths from the STO mold surface into the $Pd_{75.5}Cu_6Si_{18.5}$ film even though the step heights at the investigated location are often representing multiple unit

https://dx.doi.org/10.1021/acsami.0c14982
ACS Appl. Mater. Interfaces 2020, 12, 52908−52914

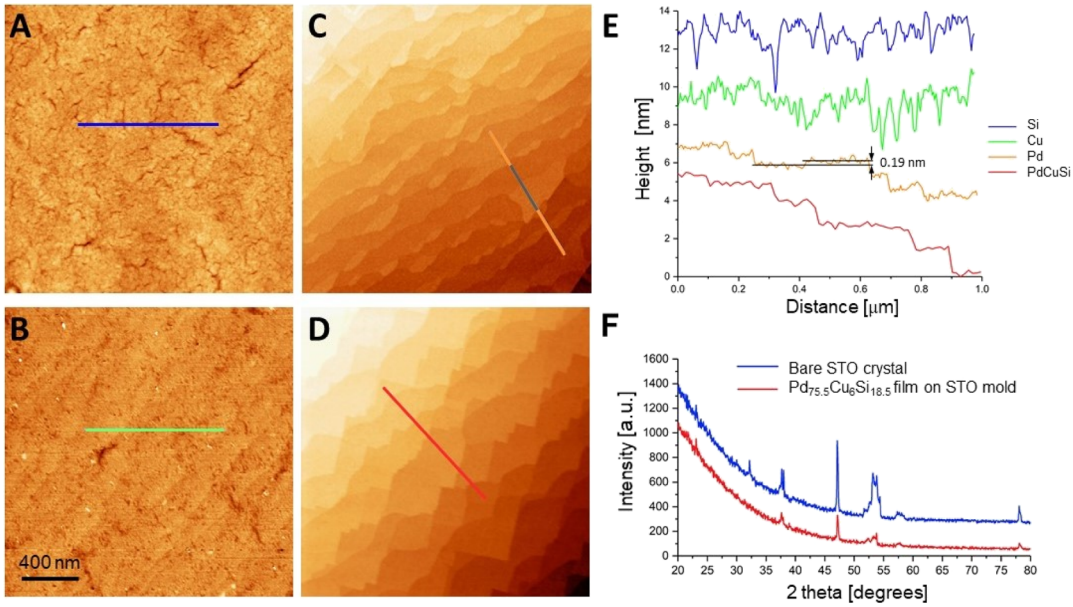

Figure 4. Relating the atomic structure to replication fidelity. (A–D) AFM images of sputter-deposited Si (A), Cu (B), Pd (C), and $Pd_{75.5}Cu_6Si_{18.5}$ (D) films after lift-off from their STO molds; all images are 2 μm × 2 μm in size. (E) Line profiles of the films taken at the locations indicated by the respectively colored lines in panels (A–D). The vertical distance between the two horizontal lines in the orange Pd line profile, whose equivalent position in (C) is highlighted with gray color, is ≈0.19 nm, which reflects the height increase obtained when adding one more layer of Pd. (F) Grazing incident X-ray diffraction spectrum acquired on the sputtered $Pd_{75.5}Cu_6Si_{18.5}$ film while it was still resting on the STO mold (i.e., before lift-off; red curve). For comparison, we also show a spectrum that was obtained on a bare STO crystal that was prepared together with the sputtering mold under the same conditions to avoid possible structural differences between the two crystals (blue curve). Because the red curve features only peaks that are already present in the blue curve, we conclude that the $Pd_{75.5}Cu_6Si_{18.5}$ film is fully amorphous.

cells.[33] For completeness, the AFM images from which the data have been taken are shown as insets with the locations of the line profiles indicated by colored lines; note that both inset images reflect zoom-outs of the areas depicted in Figure 2A,B, respectively. Analyzing the RMS roughness on the terraces, we then find, when averaging over three different squares 200 nm × 200 nm in size each, a value of (0.98 ± 0.04) Å on the film. This is slightly larger than the value obtained on the STO crystal before replication, which has been assessed, in agreement with the previously obtained results,[29] to be around 0.7 Å. This slight increase is also evident when comparing the on-terrace height fluctuations in the two line profiles.

To achieve a better understanding of what happens during lift-off, we use the results presented in Figure 3B, which shows similar line profiles for an $Au_{52}Cu_{28}Si_{20}$ replica. This time, however, the mirrored and inverted AFM image of the STO mold displayed in the upper-right inset was measured after cleavage from the film instead before sputtering took place, analogous to the procedure applied in Figure 2C. While the overall step structure is under these circumstances still well replicated, on-terrace height fluctuations are higher on the STO (blue curve) than on the $Au_{52}Cu_{28}Si_{20}$ film (red curve). This observation can be quantified comparing the STO's on-terrace roughness of (2.1 ± 0.1) Å with that of the $Au_{52}Cu_{28}Si_{20}$ film depicted in the lower-left inset, which features (0.85 ± 0.04) Å (both values were averaged using measurements from multiple squares 200 nm × 200 nm in size).

When combining the roughness analysis of the previous two paragraphs with the observations of Figure 2 and further data now shown here, we find that the roughness on the replica films of ≈0.6–1 Å tends to be slightly higher than typical values for the pristine mold surfaces (≈0.55–0.7 Å),[29] but considerably lower than what is most frequently found on the molds after separation from the sputtered film. We speculate that this is because small clusters of atoms stick to the STO during lift-off where they produce the observed increase in roughness. On the film, however, the transfer of such minute amounts of material only results in small depressions, which are largely averaged out because of the finite size of the AFM tip's apex that is unable to profile them correctly. Because the amount of materials transfer experienced during liftoff is expected to vary depending on the alloy composition used for the replica, the nature of the mold and mold temperature during deposition, as well as any possible treatment of the complete mold/replica stack before liftoff (such as heating or cooling), future work can identify mold/film combinations and/or separation protocols that minimize mass transfer if repeated subangstrom reproduction fidelity with the same mold would indeed be required. We expect that such a more systematic approach will indeed lead to improved results as in some data a roughness of less than 1 Å was already observed on the STO after separation.

To establish an upper limit for the smallest lateral dimensions that can be replicated, we are turning to Figure 3C, which shows a different location on the $Au_{50}Cu_{25.5}Ag_{7.5}Si_{17}$ film depicted in Figure 2D. Here, the STO mold featured narrow but extended pits ("trenches") that now appear on the film surface as protruding strips. Such strips, each having again heights of 3.9 Å, have in some cases widths of less than 20 nm, thereby setting an upper limit to the smallest lateral feature size. To guide the eye, we have several of them marked with two parallel lines 20 nm apart and emphasized the structural width with two arrows for better visibility. Thereby, it is important to note that because of the finite radius of the probing AFM tip's apex, the strips are recorded as being wider

https://dx.doi.org/10.1021/acsami.0c14982
ACS Appl. Mater. Interfaces 2020, 12, 52908–52914

than they actually are, which is why the features' actual lateral dimensions are expected to be considerably smaller than 20 nm. In addition, we are also limited by the width the trenches of the STO had, which was on this test sample accidental rather than purposefully set. Considering the method's fidelity in vertical direction, we extrapolate that lateral structures should be reproducible with at least nanometer accuracy.

Next, we explore the relation between replication fidelity and atomic structure, and in particular the role played by the amorphous state. Toward this end, AFM images obtained on pure metal films prepared in the same way as illustrated in Figure 1 are displayed in Figure 4A–C, each featuring one of the three constituents present in the $Pd_{75.5}Cu_6Si_{18.5}$ alloy composition used previously for the replica Figure 2B; for comparison, an image of a replica made from the $Pd_{75.5}Cu_6Si_{18.5}$ alloy is shown in Figure 4D. As the critical cooling rate for the pure metals exceeds the cooling rate during sputtering synthesis,[34] all three of the resulting pure metal films are crystalline, while grazing incident X-ray diffraction data (Figure 4F) confirm that the alloy film is amorphous.

Looking at the AFM images in more detail, we see that no features are discernible on the Si film (Figure 4A and the blue line profile in Figure 4E) and only slight hints to the existence of steps are identifiable on the Cu film (Figure 4B and the green line profile), indicating the presence of the STO surface had some influence on film growth but failed to clearly replicate any features. Because crystallization introduces a high energetic penalty for the film to accurately conform with the mold's patterned surface, such outcomes were, of course, anticipated. Defying such expectations, the film formed from pure Pd nevertheless exhibits a well-defined step structure (Figure 4C). We speculate that this is because of the coincidental quasimatch of the palladium lattice constant of ≈0.386 nm[35] with the step height of the STO crystal (≈0.391 nm),[33,35] which affords the Pd film some capability to replicate the mold's terraced surface structure with the Pd film without too much energetic cost. However, despite these favorable circumstances, the Pd film generates features not present on the STO in the form of islands that are mostly located at the top side of a step, meaning that replication is deficient. Because these islands stick out from the base terrace by ≈0.19 nm (cf. Figure 4E, orange line profile), we assume that they represent coverage with one additional layer of Pd as this distance corresponds to half of the Pd's unit cell size.

In contrast, the amorphous film formed by the $Pd_{75.5}Cu_6Si_{18.5}$ alloy (Figure 4D) produces clear terraces separated by steps measuring ≈0.39 nm or multiples of it in height (Figure 4E, red line profile), matching well with the argument made in the introduction that suggested atom sizes, interatomic distances, and packing polyhedra as the only factors limiting the imprint feature size in amorphous metallic alloys.[29] If so, the high cooling rates of sputter deposition (≈10^9 K/s) aid deposition of amorphous alloy films even when using metallic glass compositions with low glass formability. As a consequence, our technique is likely suited for many alloys that can be sputtered into an amorphous structure, which is expected to open up a huge set of available chemistry: it has been estimated that from 32 "practical elements", >10^8 distinct metallic glasses may be formed,[32] all of which could be utilized with our method.

Another favorable quality of the sputtering replication technique is its flexibility in mold choices as no force is exerted during replication and the mold barely increases in temperature. As a consequence, molds can be used that are made from a wide variety of materials, including metallic, soft, temperature-sensitive, or fragile ones, as long as a method can be found to safely separate them from the replica. Figure 5

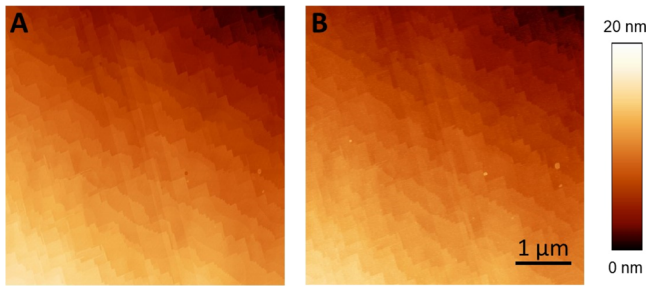

Figure 5. Replication of a temperature-sensitive metallic mold. (A) Mirrored and inverted AFM image of a mold made from $Pt_{57.5}Cu_{14.7}Ni_{5.3}P_{22.5}$ (a Pt-based BMG) before the sputtering, which was produced by nanoimprinting an STO crystal.[29] (B) AFM image of the $Au_{52}Cu_{28}Si_{20}$ film sputtered onto the Pt-BMG mold shown in (A) after cleavage. Despite the mold being temperature-sensitive and metallic, which suggests potentially higher mold-film adhesion, the replica separated easily from the mold and showed no temperature-related degradation. Both images are 5 μm × 5 μm in size.

gives an example of a metallic mold made from $Pt_{57.5}Cu_{14.7}Ni_{5.3}P_{22.5}$ BMG (Pt-BMG). The Pt-BMG was imprinted using TPF to reflect the surface structure of an STO crystal (Figure 5A)[29] before being covered with an $Au_{52}Cu_{28}Si_{20}$ film (Figure 5B). As we can see, replication of the Pt-BMG mold is successful even though the mold is temperature-sensitive (its glass transition temperature is 234 °C).[29] Similarly, we have not observed any problems with shrinkage, in contrast to reports where polymers were used for nanoimprinting.[24,25]

CONCLUSIONS

Atomic-scale replication capability has been shown by sputter deposition of amorphous metallic films, which after lift-off accurately reflect mirror images of the molds they were deposited on. During replication, the high degree of accuracy is not simply granted by the sputtering technique but relies decisively on the fact that the alloys used to sputter the films do not crystallize, which removes any dimensional limitations displayed by films that attempt to establish crystalline order. The new approach can work with a vast array of alloys, is flexible in the type of molds it can replicate, is economical because only scarce amounts of material are needed, can easily be scaled up and, using techniques similar to gilding for thin gold leaves, planar as well as nonplanar workpieces may be functionalized through nanometer-scale surface topography. Examples for applications where the new approach may be employed range from adhesion control[36] and biocompatibility[11,12] to the step-edge-directed growth of nanowires[37] and nanotubes[38−40] for nanoelectronic applications. For the latter use, specific benefits may, for example, include that (1) areas with step-edge definition may easily be combined with larger-scale structures, thereby enabling the positioning electrodes on the same substrate; (2) a "master substrate" can be replicated numerous times for scaled economic production; (3) the substrate does not exhibit any periodicity, which may allow the growth of higher-quality nanotubes and nanowires; and (4) the potentially large range of surface chemistry available may give

https://dx.doi.org/10.1021/acsami.0c14982
ACS Appl. Mater. Interfaces 2020, 12, 52908−52914

rise to further opportunities to optimize growth. As a consequence, we anticipate that this technique will find widespread application in exploring the science and technology enabled by atomic-scale imprinting.

MATERIALS AND METHODS

Sputter deposition of the alloys is carried out using a confocal DC magnetron cosputtering system (AJA International, model ATC 2200) described in ref 36. During deposition, the mold is rotated to achieve a uniform film thickness and composition. After deposition, standard microscopy glass slides are glued with EPO-TEK H72 epoxy to the top face of the sputtered metallic film. Once the glue is fully cured below the glass transition temperature of the sputtered glassy films, the molds were mechanically separated from the films with a scalpel blade. For the present study, we mostly used $SrTiO_3$ single crystals provided by MTI Corporation (Richmond, CA, USA) that were cleaned in distilled water (30 s) with ultrasonic agitation and subsequently annealed for 2 h at 1000 °C in air to expose atomically flat, (001)-oriented, TiO_2-terminated terraces separated by unit cell high steps of 3.9 Å each.[33] The exception to this is the experiment shown in Figure 5, where the mold was a $Pt_{57.5}Cu_{14.7}Ni_{5.3}P_{22.5}$ BMG that was produced by thermoplastically replicating an STO single crystal at a temperature of 270 °C; details of how this is carried out can be found in ref 29. As metallic films, we employed two different compositions for Au-based amorphous metal films ($Au_{50}Cu_{25.5}Ag_{7.5}Si_{17}$ and $Au_{52}Cu_{28}Si_{20}$, at. %) and one Pd-based alloy ($Pd_{75.5}Cu_6Si_{18.5}$), all of which were produced by DC magnetron cosputtering in 0.3 Pa argon gas of 99.999% purity at room temperature (chamber base pressure lower than 10^{-6} Pa).[41] We chose these three particular alloy compositions because of previous experience we had with their sputtering.[42] During deposition, the mold temperature stayed below 40 °C. The growth rates were ≈14 nm/min for the AuCuAgSi film (Figures 2D and 3C), ≈19 nm/min for the PdCuSi film (Figures 2B, 3A, and 4D), and ≈10 nm/min for the AuCuSi film (Figures 3B and 5B), respectively, and the material was added until the films were ≈500 nm thick.

All AFM images shown throughout this article were obtained using a Bruker Multimode AFM with Nanoscope III electronics in tapping mode with Bruker RTESPAW-300 silicon cantilevers featuring resonance frequencies ranging from 290 to 310 kHz. X-ray diffraction data have been obtained with a Rigaku SmartLab diffractometer using Cu Kα radiation.

AUTHOR INFORMATION

Corresponding Author

Udo D. Schwarz − *Department of Mechanical Engineering and Materials Science and Department of Chemical and Environmental Engineering, Yale University, New Haven, Connecticut 06511, United States;* orcid.org/0000-0002-5361-0342; Email: udo.schwarz@yale.edu

Authors

Zheng Chen − *Department of Mechanical Engineering and Materials Science, Yale University, New Haven, Connecticut 06511, United States*

Amit Datye − *Department of Mechanical Engineering and Materials Science, Yale University, New Haven, Connecticut 06511, United States;* orcid.org/0000-0002-1776-0642

Georg H. Simon − *Department of Mechanical Engineering and Materials Science, Yale University, New Haven, Connecticut 06511, United States*

Chao Zhou − *Department of Mechanical Engineering and Materials Science, Yale University, New Haven, Connecticut 06511, United States;* orcid.org/0000-0003-3259-5371

Sebastian A. Kube − *Department of Mechanical Engineering and Materials Science, Yale University, New Haven, Connecticut 06511, United States*

Naijia Liu − *Department of Mechanical Engineering and Materials Science, Yale University, New Haven, Connecticut 06511, United States*

Jingbei Liu − *Department of Mechanical Engineering and Materials Science, Yale University, New Haven, Connecticut 06511, United States;* orcid.org/0000-0003-1525-4065

Jan Schroers − *Department of Mechanical Engineering and Materials Science, Yale University, New Haven, Connecticut 06511, United States*

Complete contact information is available at: https://pubs.acs.org/10.1021/acsami.0c14982

Notes

The authors declare no competing financial interest.

ACKNOWLEDGMENTS

Help with some aspects of sample preparation and AFM imaging by Yanhui Liu and Omur Dagdeviren is gratefully acknowledged. We thank the National Science Foundation for funding through grant no. NSF CMMI-1901959. Work carried out before 6/1/2019 was supported by the Department of Energy grant no. DE-SC0016179.

REFERENCES

(1) Cabrini, S.; Kawata, S. *Nanofabrication Handbook*; CRC Press, 2012.

(2) Chou, S. Y.; Krauss, P. R.; Renstrom, P. J. Imprint Lithography with 25-Nanometer Resolution. *Science* **1996**, *272*, 85−87.

(3) Krauss, P. R.; Chou, S. Y. Nano-Compact Disks with 400 Gbit/in(2) Storage Density Fabricated Using Nanoimprint Lithography and Read with Proximal Probe. *Appl. Phys. Lett.* **1997**, *71*, 3174−3176.

(4) Nagpal, P.; Lindquist, N. C.; Oh, S.-H.; Norris, D. J. Ultrasmooth Patterned Metals for Plasmonics and Metamaterials. *Science* **2009**, *325*, 594−597.

(5) Zhang, C.; Subbaraman, H.; Li, Q.; Pan, Z.; Ok, J. G.; Ling, T.; Chung, C.-J.; Zhang, X.; Lin, X.; Chen, R. T.; Guo, L. J. Printed Photonic Elements: Nanoimprinting and Beyond. *J. Mater. Chem. C* **2016**, *4*, 5133−5153.

(6) Yu, Z.; Deshpande, P.; Wu, W.; Wang, J.; Chou, S. Y. Reflective Polarizer Based on a Stacked Double-Layer Subwavelength Metal Grating Structure Fabricated Using Nanoimprint Lithography. *Appl. Phys. Lett.* **2000**, *77*, 927−929.

(7) Schroers, J. Processing of Bulk Metallic Glass. *Adv. Mater.* **2010**, *22*, 1566−1597.

(8) Chen, X.; Zhang, L. Review in Manufacturing Methods of Nanochannels of Bio-Nanofluidic Chips. *Sens. Actuators, B* **2018**, *254*, 648−659.

(9) Kinser, E. R.; Padmanabhan, J.; Yu, R.; Corona, S. L.; Li, J.; Vaddiraju, S.; Legassey, A.; Loye, A.; Balestrini, J.; Solly, D. A.; Schroers, J.; Taylor, A. D.; Papadimitrakopoulos, F.; Herzog, R. I.; Kyriakides, T. R. Nanopatterned Bulk Metallic Glass Biosensors. *ACS Sens.* **2017**, *2*, 1779−1787.

(10) Zhang, S.; Zhang, C.; Chen, H.; Kieffer, S. J.; Neubrech, F.; Giessen, H.; Alleyne, A. G.; Braun, P. V. Selective Autonomous Molecular Transport and Collection by Hydrogel-Embedded Supramolecular Chemical Gradients. *Angew. Chem., Int. Ed.* **2019**, *58*, 18165−18170.

(11) Padmanabhan, J.; Kinser, E. R.; Stalter, M. A.; Duncan-Lewis, C.; Balestrini, J. L.; Sawyer, A. J.; Schroers, J.; Kyriakides, T. R. Engineering Cellular Response Using Nanopatterned Bulk Metallic Glass. *ACS Nano* **2014**, *8*, 4366−4375.

(12) Loye, A. M.; Kinser, E. R.; Bensouda, S.; Shayan, M.; Davis, R.; Wang, R.; Chen, Z.; Schwarz, U. D.; Schroers, J.; Kyriakides, T. R. Regulation of Mesenchymal Stem Cell Differentiation by Nanopatterning of Bulk Metallic Glass. *Sci. Rep.* **2018**, *8*, 8758.

(13) Cox, L. M.; Martinez, A. M.; Blevins, A. K.; Sowan, N.; Ding, Y.; Bowman, C. N. Nanoimprint Lithography: Emergent Materials and Methods of Actuation. *Nano Today* **2020**, *31*, 100838.
(14) Sekol, R. C.; Kumar, G.; Carmo, M.; Gittleson, F.; Hardesty-Dyck, N.; Mukherjee, S.; Schroers, J.; Taylor, A. D. Bulk Metallic Glass Micro Fuel Cell. *Small* **2013**, *9*, 2081.
(15) Guo, L. J. Recent Progress in Nanoimprint Technology and Its Applications. *J. Phys. D: Appl. Phys.* **2004**, *37*, R123−R141.
(16) Torres, C. *Alternative Lithography*; Springer Science & Business Media, 2012.
(17) Chou, S. Y.; Keimel, C.; Gu, J. Ultrafast and Direct Imprint of Nanostructures in Silicon. *Nature* **2002**, *417*, 835−837.
(18) Gates, B. D.; Whitesides, G. M. Replication of Vertical Features Smaller Than 2 Nm by Soft Lithography. *J. Am. Chem. Soc.* **2003**, *125*, 14986−14987.
(19) Hua, F.; Sun, Y.; Gaur, A.; Meitl, M. A.; Bilhaut, L.; Rotkina, L.; Wang, J.; Geil, P.; Shim, M.; Rogers, J. A.; Shim, A. Polymer Imprint Lithography with Molecular-Scale Resolution. *Nano Lett.* **2004**, *4*, 2467−2471.
(20) Xu, Q.; Mayers, B. T.; Lahav, M.; Vezenov, D. V.; Whitesides, G. M. Approaching Zero: Using Fractured Crystals in Metrology for Replica Molding. *J. Am. Chem. Soc.* **2005**, *127*, 854−855.
(21) Akita, Y.; Watanabe, T.; Hara, W.; Matsuda, A.; Yoshimoto, M. Atomically Stepped Glass Surface Formed by Nanoimprint. *Jpn. J. Appl. Phys., Part 2* **2007**, *46*, L342−L344.
(22) Elhadj, S.; Rioux, R. M.; Dickey, M. D.; DeYoreo, J. J.; Whitesides, G. M. Subnanometer Replica Molding of Molecular Steps on Ionic Crystals. *Nano Lett.* **2010**, *10*, 4140−4145.
(23) Miyake, Y.; Akita, Y.; Oi, H.; Mita, M.; Kaneko, S.; Koyama, K.; Sunagawa, K.; Tada, K.; Hirai, Y.; Yoshimoto, M. Nanoimprint Fabrication and Thermal Behavior of Atomically Ultrasmooth Glass Substrates with 0.2-Nm-Height Steps. *Jpn. J. Appl. Phys.* **2011**, *50*, 078002.
(24) Tan, G.; Inoue, N.; Funabasama, T.; Mita, M.; Okuda, N.; Mori, J.; Koyamas, K.; Kaneko, S.; Nakagawa, M.; Matsuda, A.; Yoshimoto, M. Formation of 0.3-Nm-High Stepped Polymer Surface by Thermal Nanoimprinting. *Appl. Phys. Express* **2014**, *7*, 055202.
(25) Yoshimoto, M. Sub-Nanoscale Nanoimprint Fabrication of Atomically Stepped Glassy Substrates of Silicate Glass and Acryl Polymer. *Appl. Phys. A: Mater. Sci. Process.* **2015**, *121*, 321−326.
(26) Suga, O.; Yoshimoto, M.; Okuyama, C.; Matsuda, A.; Hiroshima, H.; Takahashi, M. Atomic Step Patterning on Quartz Glass Via Thermal Nanoimprinting. *Jpn. J. Appl. Phys.* **2015**, *54*, 098001.
(27) Kumar, G.; Tang, H. X.; Schroers, J. Nanomoulding with Amorphous Metals. *Nature* **2009**, *457*, 868−872.
(28) Kumar, G.; Staffier, P. A.; Blawzdziewicz, J.; Schwarz, U. D.; Schroers, J. Atomically Smooth Surfaces through Thermoplastic Forming of Metallic Glass. *Appl. Phys. Lett.* **2010**, *97*, 101907.
(29) Li, R.; Chen, Z.; Datye, A.; Simon, G. H.; Ketkaew, J.; Kinser, E.; Liu, Z.; Zhou, C.; Dagdeviren, O. E.; Sohn, S.; Singer, J. P.; Osuji, C. O.; Schroers, J.; Schwarz, U. D. Atomic Imprinting into Metallic Glasses. *Commun. Phys.* **2018**, *1*, 75.
(30) Chen, Z.; Datye, A.; Ketkaew, J.; Sohn, S.; Zhou, C.; Dagdeviren, O. E.; Schroers, J.; Schwarz, U. D. Relaxation and Crystallization Studied by Observing the Surface Morphology Evolution of Atomically Flat Pt57.5cu14.7ni53p22.5 Upon Annealing. *Scr. Mater.* **2020**, *182*, 32−37.
(31) Bordeenithikasem, P.; Sohn, S.; Liu, Z.; Schroers, J. Protocols for Multi-Step Thermoplastic Processing of Metallic Glasses. *Scr. Mater.* **2015**, *104*, 56−59.
(32) Li, Y.; Zhao, S.; Liu, Y.; Gong, P.; Schroers, J. How Many Bulk Metallic Glasses Are There? *ACS Comb. Sci.* **2017**, *19*, 687−693.
(33) Dagdeviren, O. E.; Simon, G. H.; Zou, K.; Walker, F. J.; Ahn, C.; Altman, E. I.; Schwarz, U. D. Surface Phase, Morphology, and Charge Distribution Transitions on Vacuum and Ambient Annealed Srtio3(100). *Phys. Rev. B* **2016**, *93*, 195303.
(34) Zhong, L.; Wang, J.; Sheng, H.; Zhang, Z.; Mao, S. X. Formation of Monatomic Metallic Glasses through Ultrafast Liquid Quenching. *Nature* **2014**, *512*, 177−180.
(35) Davey, W. P. Precision Measurements of the Lattice Constants of Twelve Common Metals. *Phys. Rev.* **1925**, *25*, 753−761.
(36) Vajpayee, S.; Khare, K.; Yang, S.; Hui, C.-Y.; Jagota, A. Adhesion Selectivity Using Rippled Surfaces. *Adv. Funct. Mater.* **2011**, *21*, 547−555.
(37) Tsivion, D.; Schvartzman, M.; Popovitz-Biro, R.; von Huth, P.; Joselevich, E. Guided Growth of Millimeter-Long Horizontal Nanowires with Controlled Orientations. *Science* **2011**, *333*, 1003−1007.
(38) Kocabas, C.; Hur, S.-H.; Gaur, A.; Meitl, M. A.; Shim, M.; Rogers, J. A. Guided Growth of Large-Scale, Horizontally Aligned Arrays of Single-Walled Carbon Nanotubes and Their Use in Thin-Film Transistors. *Small* **2005**, *1*, 1110−1116.
(39) Ismach, A.; Segev, L.; Wachtel, E.; Joselevich, E. Atomic-Step-Templated Formation of Single Wall Carbon Nanotube Patterns. *Angew. Chem., Int. Ed.* **2004**, *43*, 6140−6143.
(40) Kang, S. J.; Kocabas, C.; Ozel, T.; Shim, M.; Pimparkar, N.; Alam, M. A.; Rotkin, S. V.; Rogers, J. A. High-Performance Electronics Using Dense, Perfectly Aligned Arrays of Single-Walled Carbon Nanotubes. *Nat. Nanotechnol.* **2007**, *2*, 230−236.
(41) Ding, S.; Liu, Y.; Li, Y.; Liu, Z.; Sohn, S.; Walker, F. J.; Schroers, J. Combinatorial Development of Bulk Metallic Glasses. *Nat. Mater.* **2014**, *13*, 494−500.
(42) Bordeenithikasem, P.; Liu, J.; Kube, S. A.; Li, Y.; Ma, T.; Scanley, B. E.; Broadbridge, C. C.; Vlassak, J. J.; Singer, J. P.; Schroers, J. Author Correction: Determination of Critical Cooling Rates in Metallic Glass Forming Alloy Libraries through Laser Spike Annealing. *Sci. Rep.* **2018**, *8*, 17898.

https://dx.doi.org/10.1021/acsami.0c14982
ACS Appl. Mater. Interfaces 2020, 12, 52908−52914